STM JOURNALS

Journal of
Polymer & Composites

ISSN: 2321-2810 (Online)
ISSN: 2321-8525 (Print)
Volume 13, Issue 6, 2025
DOI (Journal): 10.37591/JoPC

https://journals.stmjournals.com/jopc/

Research JoPC

An Ultraviolet-Curable Nano Cerium Oxide Coating and Its Anti Ultraviolet /Blue Light Properties

Guoyao Li[1], Yihua Sun[2], Rong Zhong[3,*]

Abstract

An ultraviolet (UV)-curable nano cerium oxide (CeO_2) coating with enhanced blue light and UV shielding properties, prepared using an ultrasonic blending method, is presented. This study systematically investigated the optimal synthesis conditions for nano CeO_2, as well as the effects of UV intensity and CeO_2 concentration on the curing kinetics and blue/UV light shielding performance of the UV-curable nanocomposite. The results indicate that the synthesized nano CeO_2 exhibited improved mechanical properties and reduced agglomeration compared to commercially available CeO_2. Furthermore, the UV-cured PUA/CeO_2 composite demonstrated superior reflection and scattering capabilities for both blue and UV light compared with composites containing commercial CeO_2 at equivalent additive concentrations. These findings highlight the potential of the proposed nanocoating for applications requiring robust UV and blue light shielding performance. When the nano CeO_2 content is 4%, the shielding rates of the coating for UV and blue light are approximately 40% and 34%, respectively. The cured composites have excellent mechanical properties. Its pencil hardness can reach 4H, adhesion, 4B, flexibility, 5 and has good abrasion resistance. This indicates its potential for industrial applications. The UV cured nano-coating is expected to be used in the field of electronic products, such as display screen protective layers for mobile phones, ipad, tablets, etc., to reduce the damage to human vision caused by long-term use of these products.

Keywords: UV-curable coating; nano CeO_2; UV, blue light and shielding

INTRODUCTION

In the past decade, ultraviolet (UV)-curable coatings, as environmentally friendly coating products, have developed rapidly [1–3], with UV-curable organic/inorganic hybrid coatings being increasingly applied [4–6]. UV-curing technology offers advantages such as high transparency, moisture resistance, and resistance to chemical environments [7]. Moreover, compared with traditional solvent-evaporation-cured coatings, UV-curable coatings have the advantage that almost all formulations participate in the curing reaction, significantly reducing waste, while achieving faster curing speeds and lower energy consumption [7–8]. Therefore, UV-curable coatings are regarded as green coatings with five 'E' characteristics: efficiency, environmental protection, energy saving, economy, and multifunctionality [9–12]. They are widely used in fields such as 3D printing, aerospace, and the medical industry [13–15].

With technological advancement, reliance on electronic products has increased. However, ultraviolet/blue light in the 201–450 nm range emitted by their screens can penetrate the lens and reach the retina directly, causing visual damage [16]. Consequently, this harmful radiation has driven the development of more effective UV/blue

***Author for Correspondence**
Rong Zhong
E-mail: zhongr@nchu.edu.cn (R. Zhong)

[1,2]Student, Department of Materials and Chemistry, School of Environmental & Chemical Engineering, Nanchang Hangkong University, Nanchang, China
[3]Associate Professor, Department of Materials and Chemistry, School of Environmental & Chemical Engineering, Nanchang Hangkong University, Nanchang, China

Received Date: August 25, 2025
Accepted Date: September 20, 2025
Published Date: October 18, 2025

Citation: Guoyao Li, Yihua Sun, Rong Zhong. An Ultraviolet-Curable Nano cerium Oxide Coating and Its Anti Ultraviolet /Blue Light Properties. Journal of Polymer & Composites. 2025; 13(6): 306–324p.

light shielding materials [17–20]. Sukshun et al. [21] employed a benzotriazole UV absorber (i.e., UV326) and transparent yellow pigment as functional additives, incorporating them into plasticized polyvinyl chloride by melt blending to produce a high-transparency film capable of blocking UV/high-energy blue light. This film demonstrated more than 99% shielding effectiveness in the ultraviolet and high-energy blue regions. Li et al. [22] synthesized cadmium sulfide (CdS) quantum dots with cubic and hexagonal crystal lattices via a solvothermal method and incorporated them into a poly(N,N-dimethylacrylamide) matrix to prepare transparent nanocomposite films. These nanocomposite films exhibited a narrow blue light absorption transition band, with the wavelength range corresponding to 5–80% maximum transmittance being only 20 nm (440–460 nm). Chunchun Han et al.[23] developed epoxy-ZnO/CdS (EP-ZC) nanocomposites capable of blocking UV and blue radiation. These nanocomposites, containing 0.3 wt% ZnO, blocked almost all ultraviolet light between 200–400 nm and more than 80% of blue light between 400–450 nm.

Nano-CeO_2, as an important UV-absorbing material, demonstrates excellent UV absorption compared to TiO_2 and ZnO, while maintaining higher transparency to visible light[24, 25]. Liu et al. [26] incorporated CeO_2 nanoparticles into a polystyrene matrix to enhance UV shielding performance. Yu et al. [27] coated silicate microspheres (SMSs) with CeO_2 to synthesize core–shell particles (SMS–CeO_2), thereby improving the blue light shielding performance of polycarbonate composites and enabling greater transmission of other visible light. However, commercially available CeO_2 nanoparticles tend to aggregate easily and are challenging to process due to their high surface energy and reactivity [28–29]. Numerous studies have investigated methods to reduce agglomeration, including chemical precipitation [30], sol–gel, hydrothermal synthesis [31], and microemulsion techniques[32], all of which have been shown to effectively disperse CeO_2 nanoparticles and reduce aggregation. Resently, many rein hybrid polymer composities was investigated [33–37].

Currently, few studies have reported the direct dispersion of treated nano-CeO_2 into UV-curable coatings to achieve blue light shielding. Jyh et al.[38] developed blue light-blocking glass that reduces light transmittance below 460 nm while maintaining high transmittance at a wavelength of 550 nm by doping TiO_2, CeO_2, and Bi_2O_3 into a Na_2O–CaO_2–Al_2O_3–SiO_2 glass composition. Additionally, nano-CeO_2 is frequently employed in UV-blocking coatings due to its strong UV-shielding capability [39, 40]. Mohammad et al. [41] prepared coatings with multiple self-healing and UV-blocking properties by combining polyols with suitable CeO_2, enabling applications in outdoor products.

This study aims to prepare a highly wear-resistant and stable UV/blue light-blocking photocurable organic/inorganic hybrid coating. Using the sol–gel method, commercially available agglomerated nano-CeO_2 is dispersed. This approach enables uniform mixing at the molecular level at relatively low temperatures and facilitates the doping of trace elements, offering the advantage of a low preparation temperature. The dispersed nano-CeO_2 is subsequently incorporated into a polyurethane acrylate system to produce a UV-curable polyurethane acrylate/CeO_2 composite material for UV and blue light shielding. This type of coating effectively provides shielding against both blue and UV light. Furthermore, the shielding rates of polyurethane acrylate/CeO_2 composite materials across various visible light ranges (280–400 nm) and ultraviolet light (400–700 nm) are also investigated.

METHODS

Materials

Aliphatic polyurethane acrylate (SD7549) was purchased from Guangzhou Songda New Materials. Trimethylolpropane triacrylate (TPGDA), trimethylolpropane triacrylate (TMPTA), 1,6-hexanediol diacrylate (HDDA), and pentaerythritol triacrylate (PETA) were purchased from Guangzhou Boxing New Materials. 1-Hydroxycyclohexyl phenyl ketone (Irgacure184) was purchased from Tianjin Jiuri New Materials. Nano cerium oxide was purchased from Aladdin. Toluene and ethyl acetate were purchased from Xilong Scientific. Cerium oxide hexahydrate ($CeO_2 \cdot 6H_2O$) was purchased from Macklin, Shanghai. Citric acid was purchased from Tianjin Zhonglian Chemical Reagents.

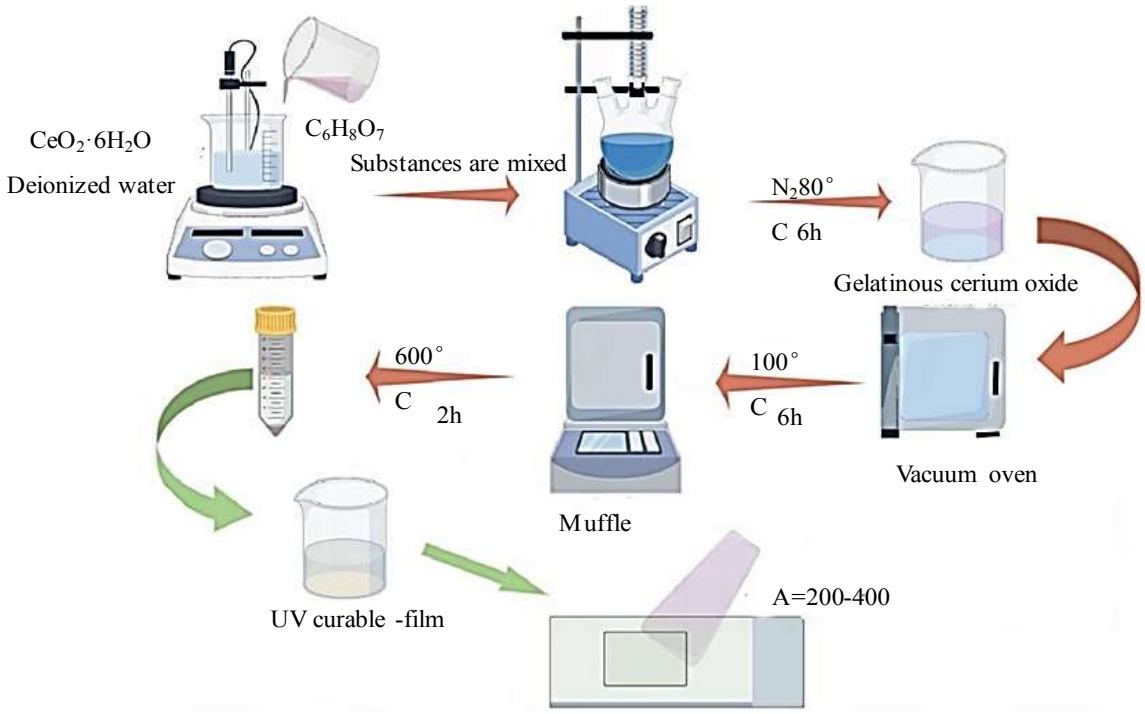

Figure 1. The preparation of UV-curable film.

$$Ce(NO_3)_3\ 6H_2O + C_6H_8O_7 \xrightarrow[100°C]{\triangle} [Ce(C_6H_5O_7)]\ nH_2O + 3HNO_3 + (6-n)H_2O \quad 1$$

$$[Ce(C_6H_5O_7)]\ nH_2O \xrightarrow[500°C]{\triangle} CeO_2 + 6CO_2\uparrow + (n+3)H_2O\uparrow \quad 2$$

Figure 2. Reaction equation for nano-oxide of Nano- CeO_2.

Synthesis of Nano CeO_2

Weigh 5.32 g of CeO_2•$6H_2O$ and 7.06 g of citric acid into a beaker, then dissolve them in 200 mL of deionized water. Stir the mixture thoroughly using a magnetic stirrer. Transfer the homogeneous solution into a three-necked flask and allow the reaction to proceed until a sol forms. Collect the resulting gel and dry it in an oven at 100°C for 4 hours. Place the dried gel in a corundum crucible and sinter it in a muffle furnace at the specified temperature for two hours.

Figure 2 shows the reaction equation between Ce $(NO_3)_3 \cdot 6H_2O$ and citric acid. Reaction 1 showed that citric acid formed a stable complex with Ce^{3+}, and the molar ratio of metal ions to citric acid was regulated, which delayed the hydrolysis rate and controlled the particle morphology. During vacuum drying at 100°C, the complex is gradually hydrolyzed to form a hydrated cerium dioxide precursor, which is finally sintered and dehydrated in a (Reaction 2) muffle furnace to form CeO_2 crystals.

The molar ratio, reaction temperature, sintering temperature and other factors of Ce $(NO_3)_3 \cdot 6H_2O$ and citric acid were investigated to obtain the optimal reaction conditions of Nano CeO2.The experiment was carried out according to the above steps. The molar ratio of Ce $(NO_3)_3$ • 6H2O to citric acid was varied at 1:2, 1:3, 1:4, and 1:5, while the reaction temperature was adjusted to 75℃, 80℃, 85℃, and 90℃. Additionally, the sintering temperature was modified to 500℃, 600℃, 700℃, and 800℃ to study their effects on the final product.

Preparation of UV-Cured Nanocomposite Coating Film

The preparation of UV-curable film can be seen Figure 1, under light-protected conditions, specified amounts of SD7549, TPGDA, and photoinitiator 184 were added into a disposable plastic beaker, using ethyl acetate as the diluent. The components were then mixed thoroughly and ultrasonically dispersed for 30 minutes. After complete dissolution, the mixture was applied using a 30-mesh wire-wound bar and baked in an oven at 80°C for 40 seconds. The coating was cured with a handheld UV radiation curing machine. After curing, the coating film thickness was measured using a digital display thickness gauge. It was observed that when the ratio of active ingredient to diluent was 3:7, the resulting film thickness was 3 μm. Here, the active ingredient refers to the components involved in the crosslinking reaction during UV curing, whereas the diluent acts solely as a solvent and does not participate in the reaction. Finally, the nano-CeO_2 was dried in an oven at 80°C for 12 hours, then incorporated into the optimized UV-curing formulation at a defined mass percentage of the total composition. The concentration was adjusted to the desired level using the diluent, ultrasonically dispersed, applied with a 30-mesh wire-wound bar, and cured using a handheld UV radiation curing machine.

Testing and Characterization of Nano-CeO_2 and Composites

The surface drying time of the coating film was measured according to the finger-touch method in GB/T1728-1979; adhesion was evaluated in accordance with GB/T9286-1998; and hardness was tested following GB/T6739-2006.

A Nova SEM 450 field emission scanning electron microscope (SEM) was used to analyze the surface morphology of the rare earth complexes. A cotton swab was dipped into a small amount of the sample and applied onto conductive adhesive. The sample surface was gold sputtered and then placed in the instrument for scanning to observe the apparent morphology and dispersion state of the nano-oxides.

A Cu-Kα X-ray diffractometer (XRD) was employed to characterize and analyze the crystal phases of the rare earth complexes. The test was conducted at a voltage of 40 kV and a current of 40 mA, with a 2θ scanning angle range of 5° to 80°.

A Nicolet Magna 380 Fourier transform infrared spectrometer (U.S.) was used to determine and characterize the structure of the rare earth complexes via the KBr pellet method. The sample structure was identified based on the absorption peaks of various functional groups in the infrared spectrum, within a wavenumber detection range of 400–4000 cm−1.

A TG-209 thermogravimetric analyzer was used to measure the thermal stability and structural composition of the samples. The test was performed under a nitrogen atmosphere, with a temperature range from 50°C to 1000°C, a heating rate of 10°C/min, and a gas flow rate of 100.0 mL/min. Data were recorded at 0.5-second intervals.

A UV-2550 ultraviolet–visible spectrophotometer (Shimadzu, Japan) was used to evaluate the response of the coating film to ultraviolet light irradiation, with a scanning range of 200–500 nm.

RESULTS AND DISCUSSION

Effect of Different Molar Ratios on the Synthesis of Nano- CeO_2

Figures 3 (a), (b), (c), and (d) display the scanning electron microscope (SEM) images of nano- CeO_2 synthesized with different molar ratios of $CeO_2 \cdot 6H_2O$ to citric acid at 1:2, 1:3, 1:4, and 1:5, respectively. At a molar ratio of 1:2, a fluffy layered crystal structure is formed, with significant secondary agglomeration. At 1:3, the particle size is uniform, the CeO_2 particles are the smallest, with well-defined particle boundaries and no significant agglomeration. At 1:4, both the crystals and particles become larger, the particle boundaries become blurred, the particle size increases, and crystallinity decreases. At 1:5, the crystals appear as flaky structures, with further enlargement of particle size and even poorer crystallinity. This is due to the fact that the sol-gel synthesis of nano-CeO_2 is a hydrolytic polymerization process. Citric acid, being a strong tricarboxylic acid and a multidentate ligand, contains four coordination groups: three carboxyl groups and one hydroxyl group. The coordination mode varies

with the amount of citric acid added. Excessive citric acid in the reaction system results in a large amount of free citric acid, which ultimately affects the particle size.

Figure 4 shows the XRD powder diffraction patterns of $CeO_2 \cdot 6H_2O$ and citric acid at different molar ratios. It can be seen that the diffraction peaks correspond to the standard PDF card, indicating that the synthesized material is nano-CeO_2, with clear and sharp peaks and no impurity peaks. As the molar ratio increases, the crystallinity gradually decreases. Based on the combined results from SEM and XRD analyses, the optimal feed ratio is determined to be 1:3.

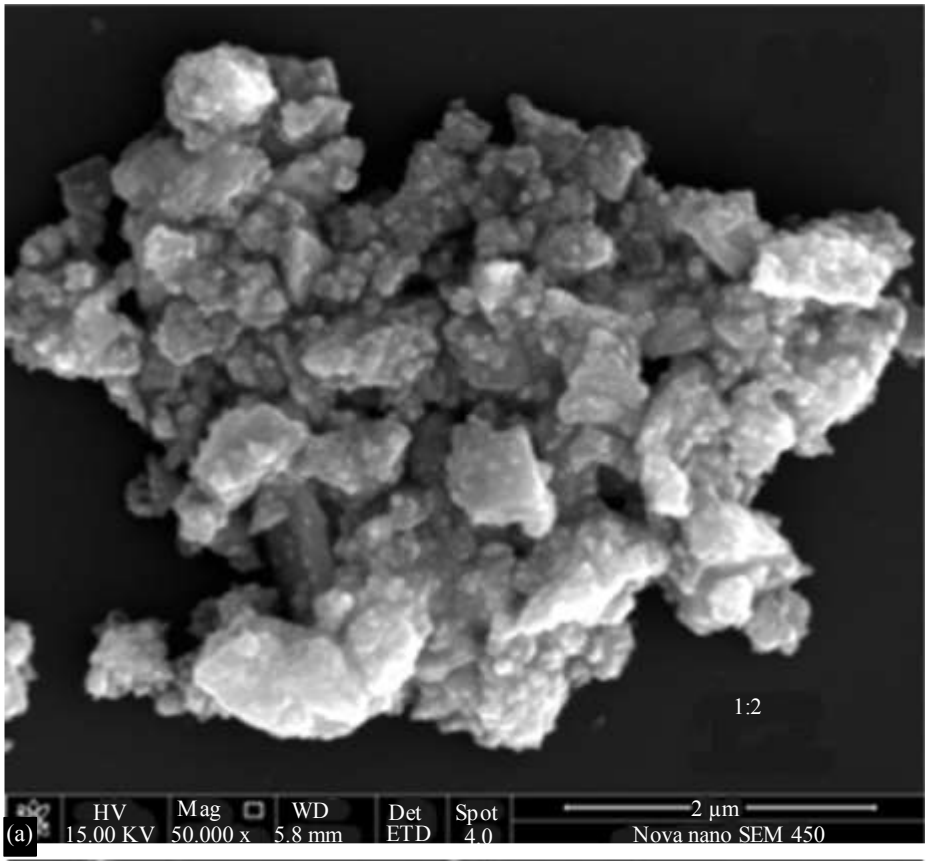

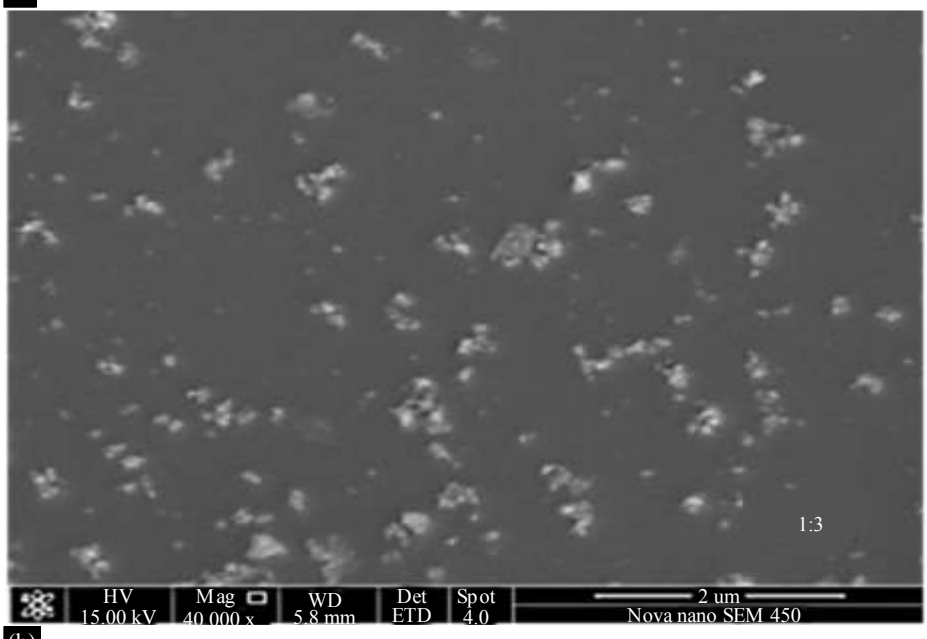

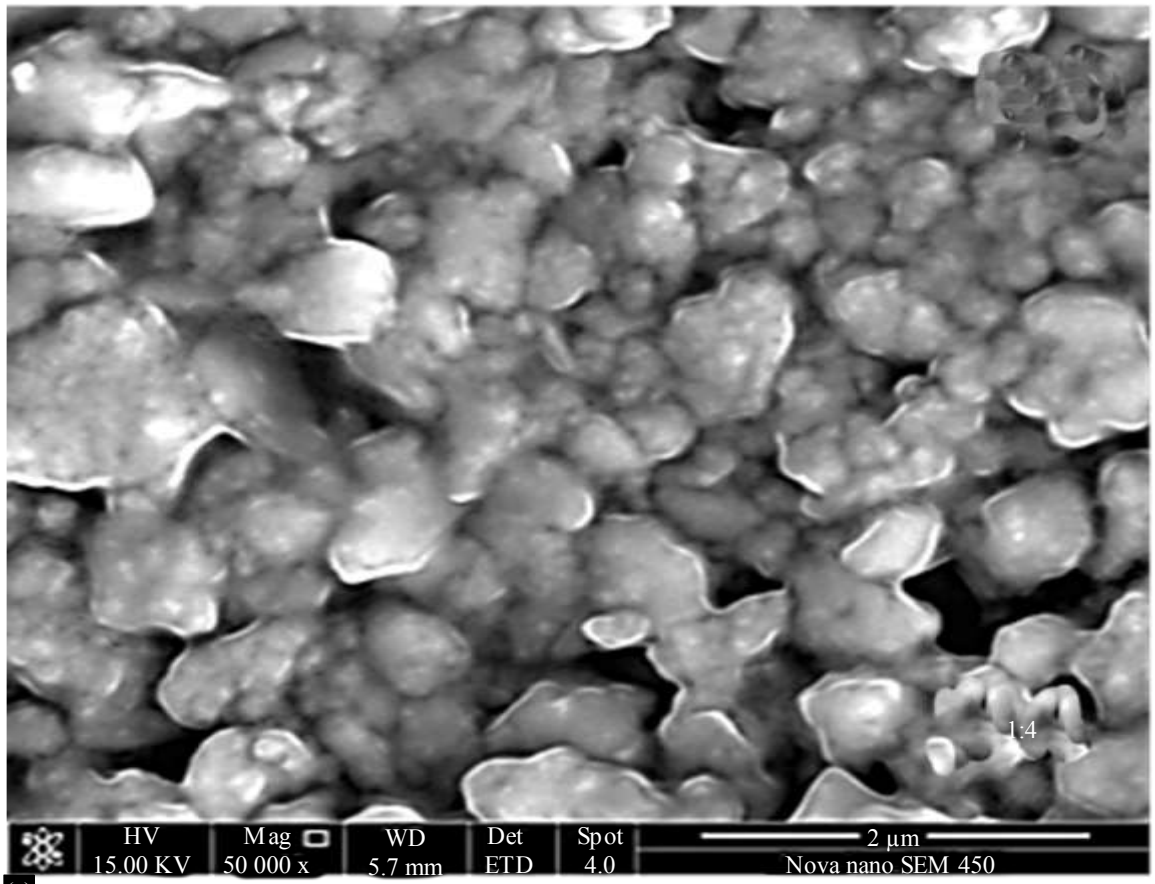

(c)

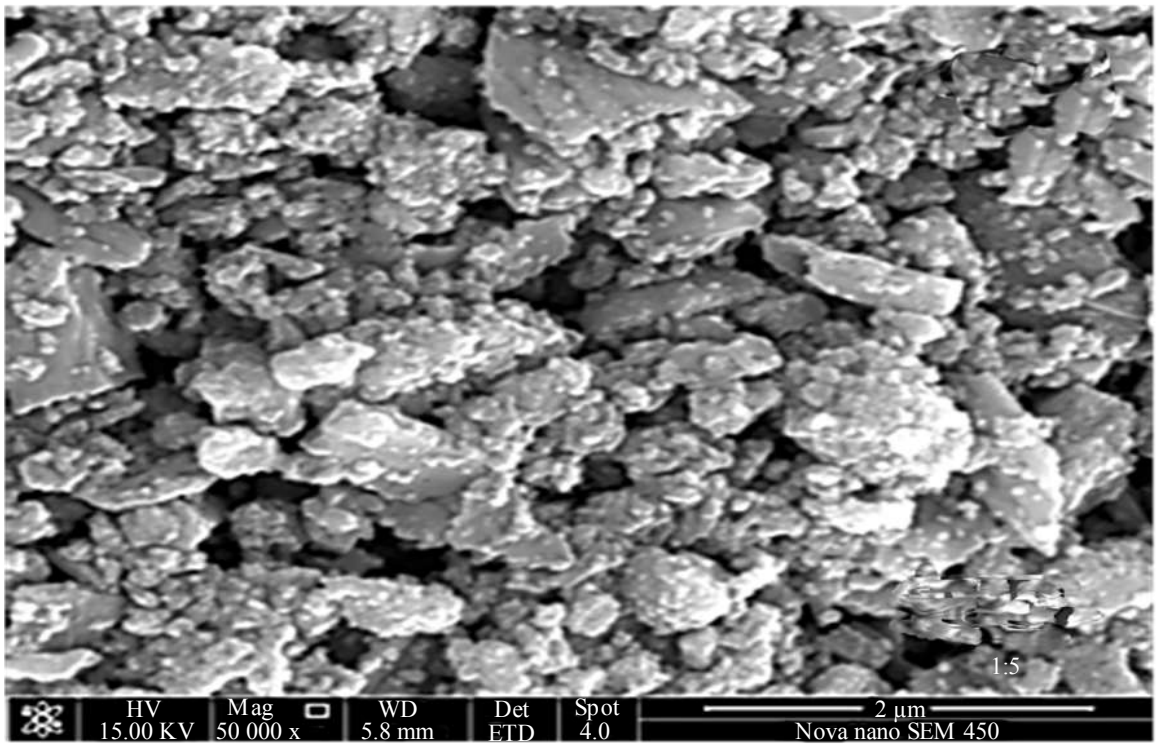

Figure 3. (a), (b), (c), and (d) illustrate the effects of different molar ratios on the synthesis of nano-CeO2.

(d)

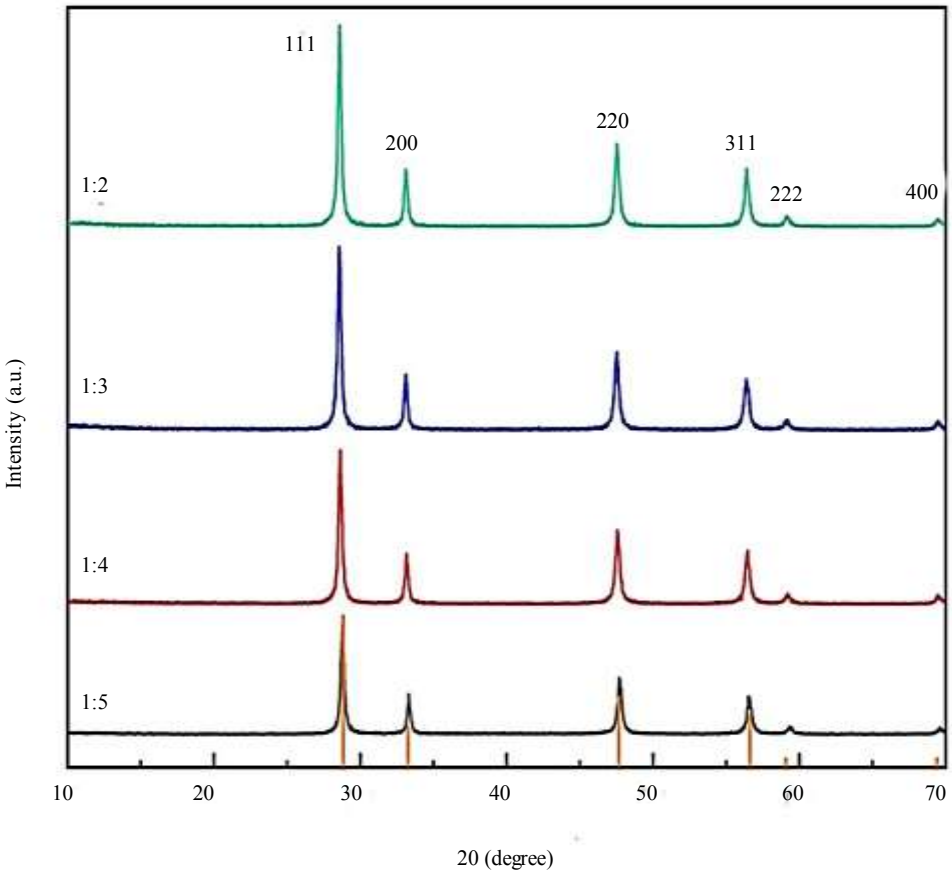

Figure 4. XRD patterns of nano-CeO_2 synthesized at different molar ratios.

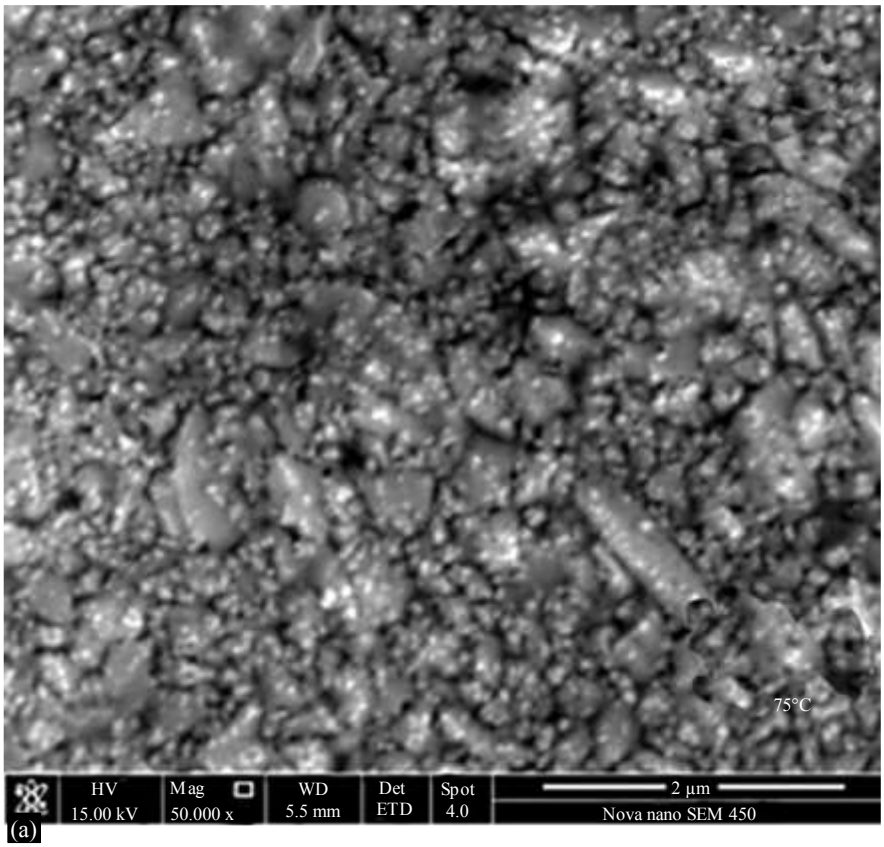

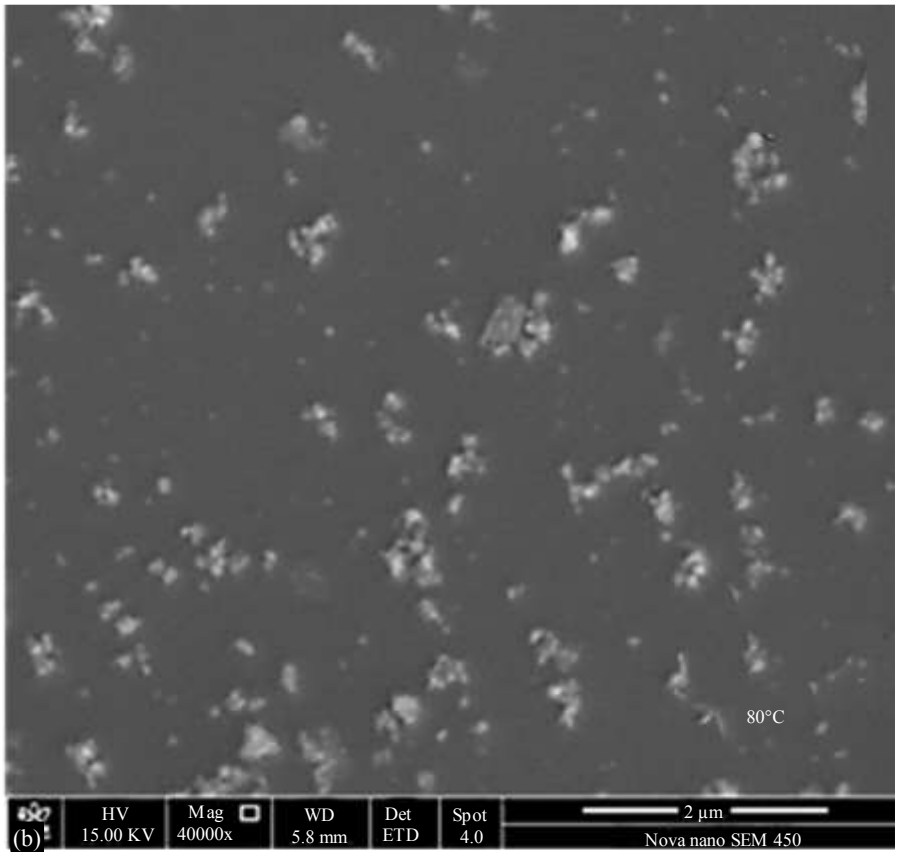

(b)

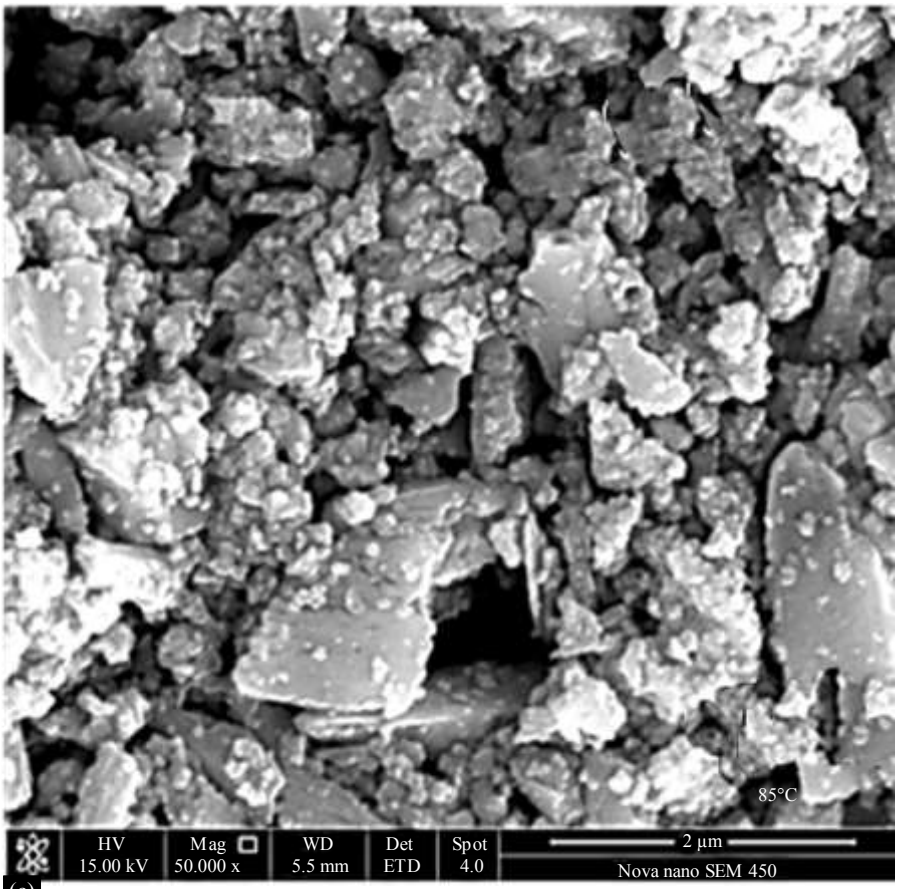

(c)

Figure 5. The effect of different reaction temperatures on the synthesis of nano-CeO_2.

Effect of reaction Temperature on the Synthesis of Nano-CeO_2

The molar ratio of CeO_2•$6H_2O$ to citric acid was fixed at 1:3. At reaction temperatures of 75°C, 80°C, 85°C, and 90°C, the gelation times were 80, 65, 50, and 40 minutes, respectively. The results indicate that increasing the reaction temperature gradually reduces gelation time. This is because, at higher temperatures, the number of activated molecules per unit time increases, accelerating the gelation process.

Figures 5(a)–(d) show the SEM images of nano-CeO_2 synthesized at 75°C, 80°C, 85°C, and 90°C, respectively. At 75°C, the synthesized nano-CeO_2 crystals are a mixture of rod-shaped and spherical structures, with no apparent agglomeration but relatively large particle size. At 80°C, the nano-CeO2 exhibits the smallest particle size, uniform particle morphology, and no significant agglomeration. In Figures 3(c) and 3(d), as the temperature continues to increase, crystallinity decreases progressively. This is attributed to grain growth at higher temperatures, which leads to more complex crystal morphologies and increased particle size.

Figure 6 presents the XRD patterns of nano-CeO_2 synthesized at different reaction temperatures. The diffraction peaks correspond to the standard CeO_2 PDF card, confirming successful synthesis. At a reaction temperature of 80°C, the nano-CeO_2 shows the smallest particle size, the most uniform distribution, and no evidence of agglomeration.

Effect of Sintering Temperature on the Synthesis of Nano- CeO_2

Figures 7(a)–(d) present the SEM images of nano-CeO_2 synthesized at sintering temperatures of 500°C, 600°C, 700°C, and 800°C, respectively. The results indicate that as the sintering temperature increases, the particle size of the product gradually grows, leading to a darker product color and reduced light absorbance. At 500°C, the reaction product exhibits the smallest particle size with no noticeable agglomeration. At 700°C, the product develops into spherical crystals with evident agglomeration. At both 700°C and 800°C, the crystals further evolve into sheet-like structures.

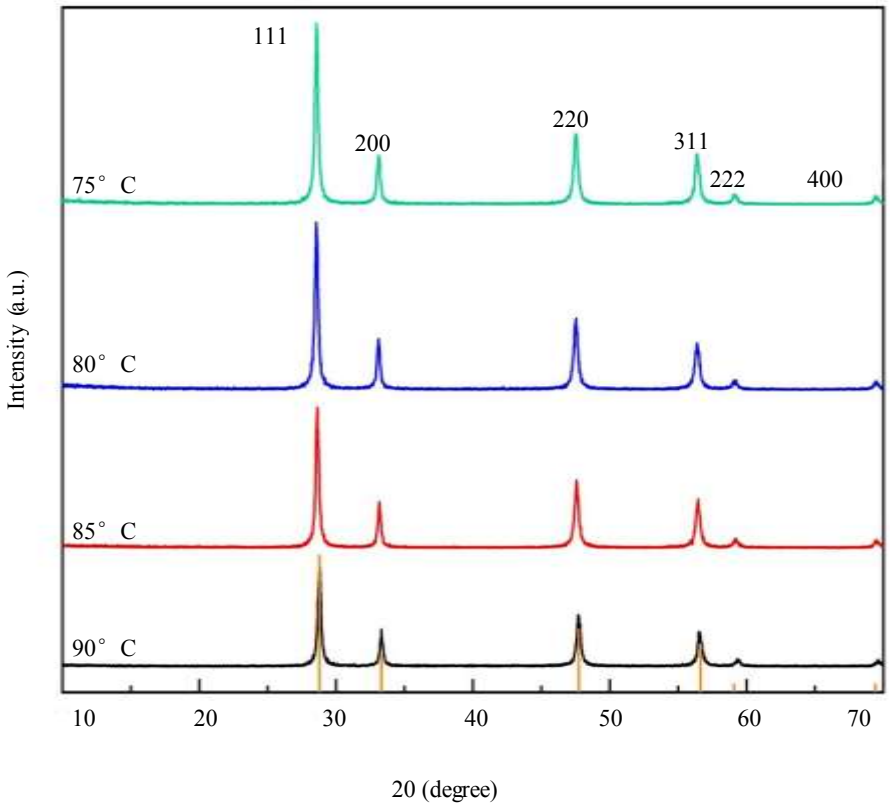

Figure 6. XRD patterns showing the effect of different reaction temperatures on the synthesis of nano-CeO_2.

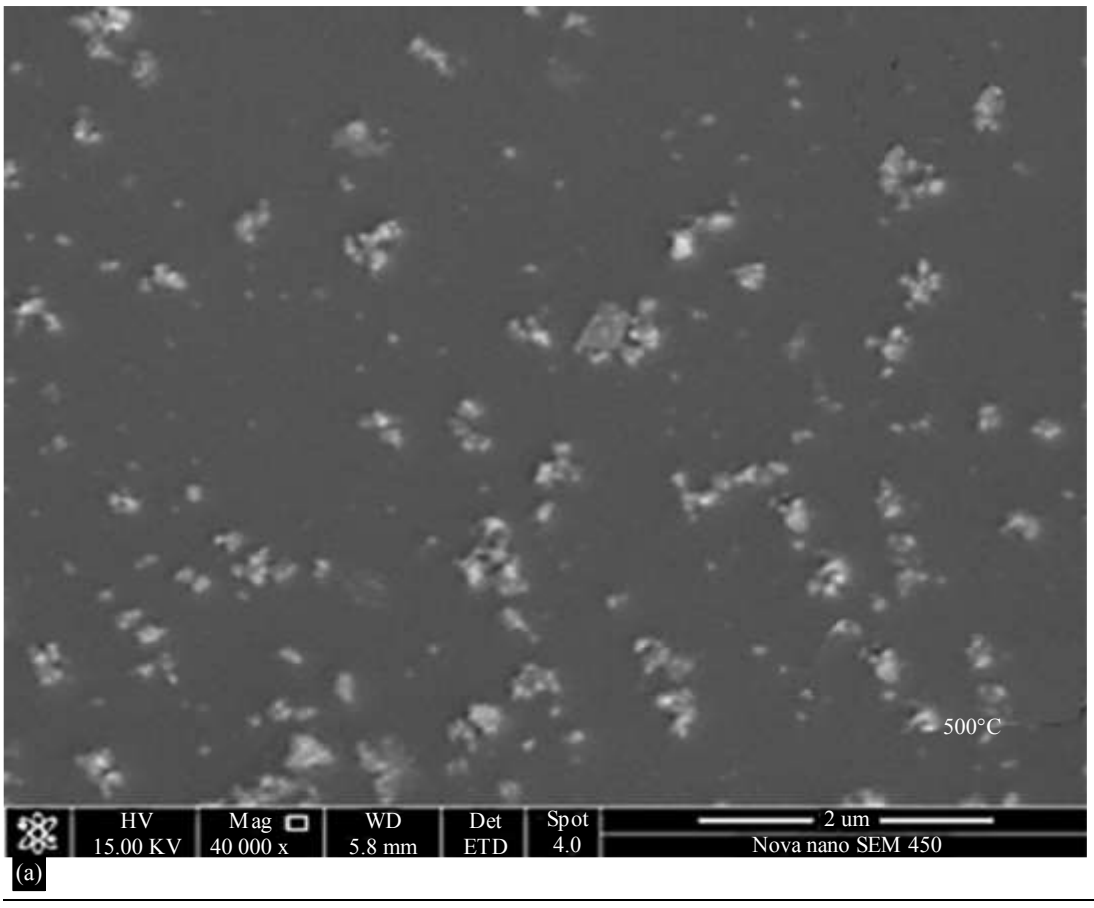

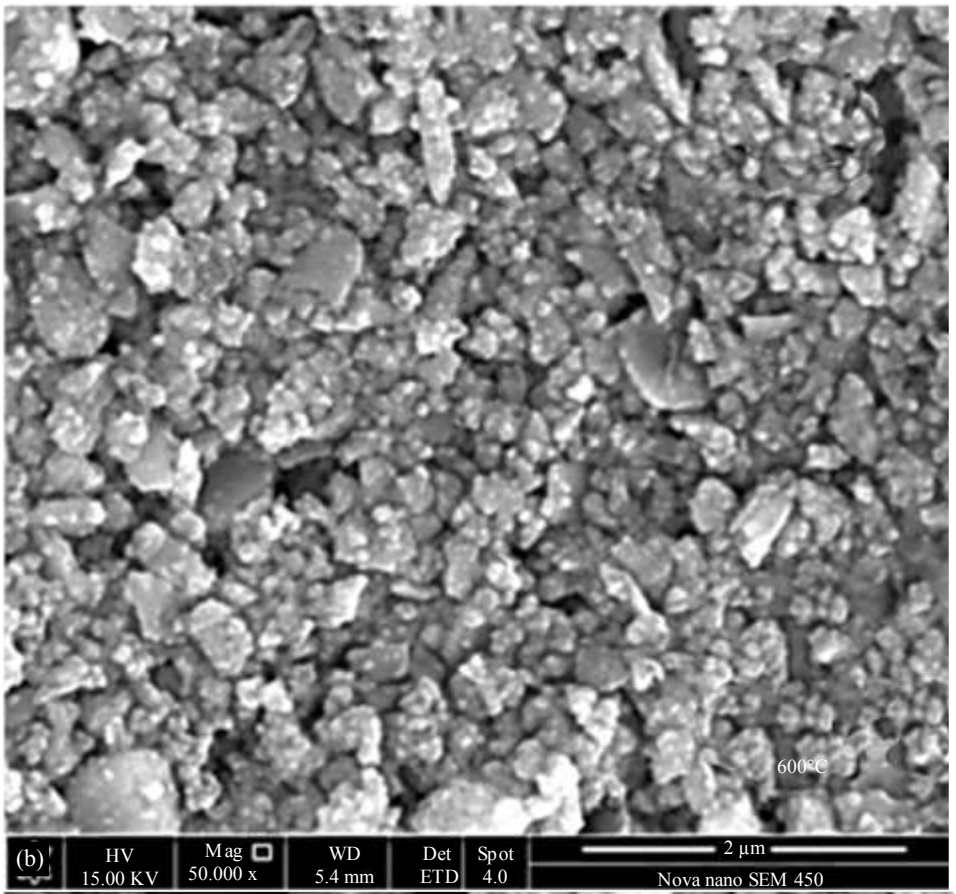

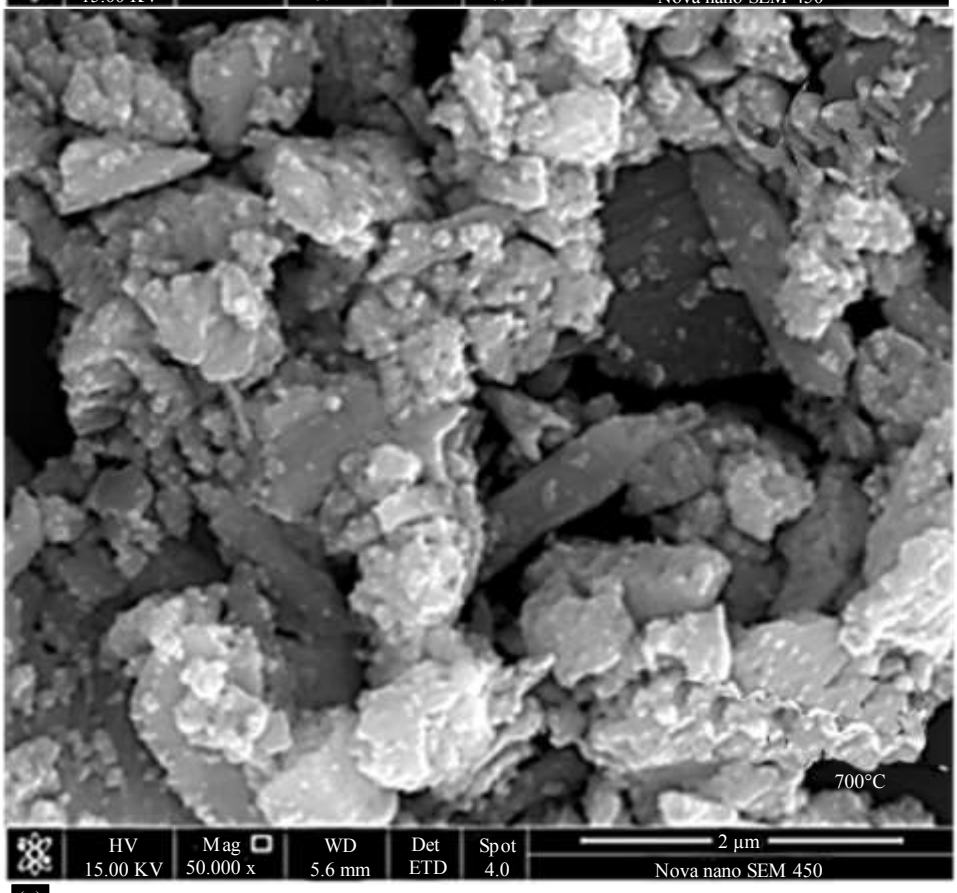

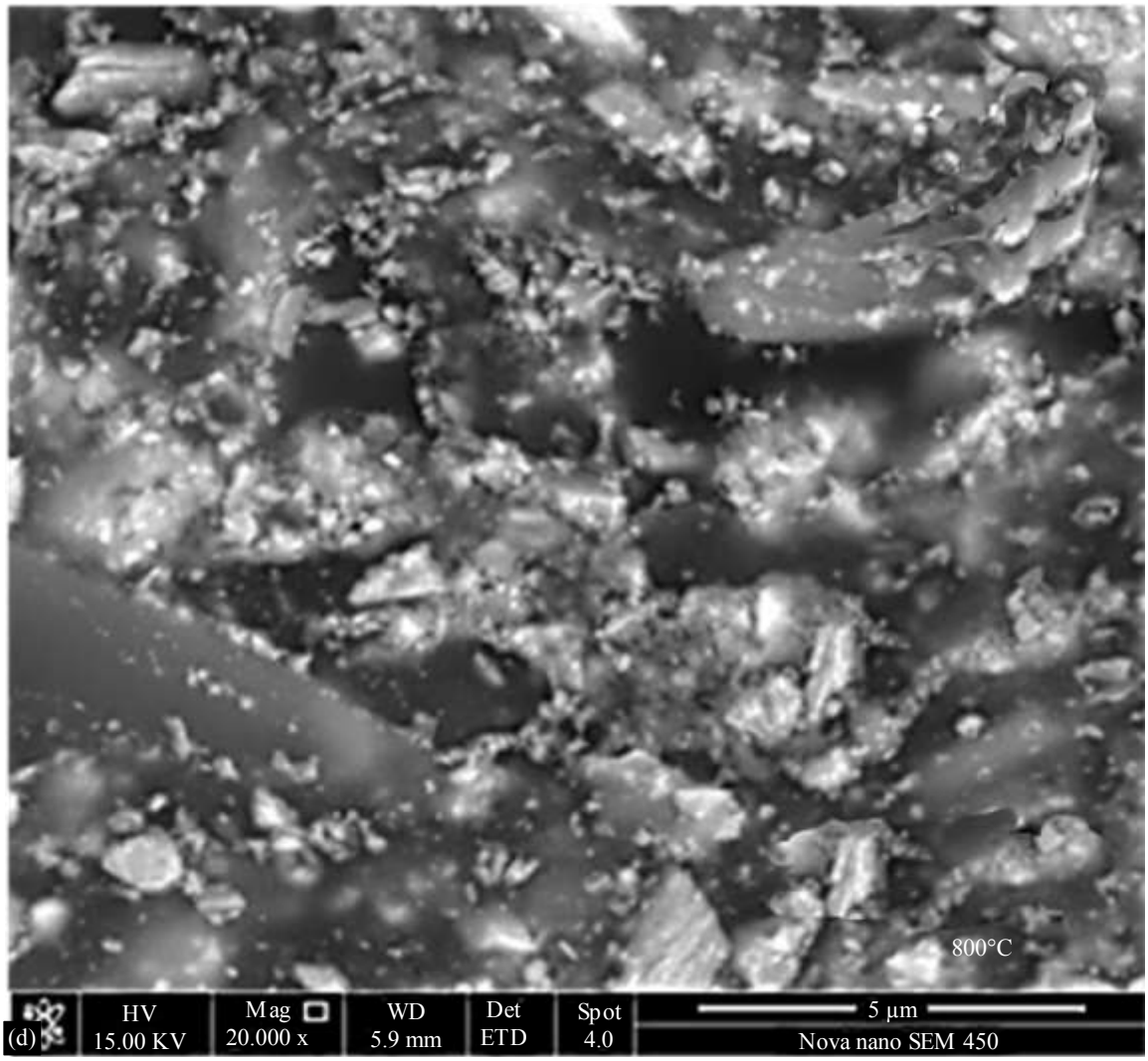

Figure 7. The effect of different sintering temperatures on the synthesis of nano- CeO_2.

Stability and Mechanical Properties of the hybrid Coating

Table 1 presents the stability test results of nano-CeO_2 in the hybrid coating. The findings show that when the nano-CeO_2 content exceeds 4%, significant sedimentation occurs after 12 hours of standing. Therefore, in subsequent studies, the addition of modified nano-CeO_2 should be controlled within the range of 0–4% to prepare hybrid coatings and evaluate their performance.

Table 1. Effect of different content of nano CeO_2 on the stability performance of coatings.

CeO_2 (%)	**Standing time**				
1	2hNo	4hNo	12h No	24hNo	36hNo
1.5	No	No	No	No	No
2	No	No t	No	No	No
2.5	No	No	No	No	No
3	No	No	Not	No	Slight sediment
4	No t	No	No	Slight sediment	Slight sediment
5	Slight sediment	Slight sediment	Significant sediment	Significant sediment	Significant sediment
1	No	No	No	No	No

Table 2. Effect of different content of nano CeO_2 on the mechanical performance of coatings.

CeO_2 content (%)	Hardness	Flexibility (T)	Adhesion (grade)	Abrasion resistance	Full cure time (s)
0	2H	9	4B	Slight scratches	7
1	2H	8	4B	Slight scratches	7
1.5	3H	8	4B	No scratches	7
2	3H	7	4B	No scratches	7
2.5	4H	6	4B	No scratches	8
3	4H	6	4B	No scratches	8
3.5	4H	6	4B	No scratches	9
4	4H	5	4B	No scratches	9

Table 2 summarizes the mechanical performance test results of the nano-CeO_2 hybrid coating. As the nano-CeO_2 content increases, the coating's wear resistance and hardness improve markedly, whereas flexibility decreases. This is attributed to the presence of metal oxide particles, which are more rigid than the organic coating matrix, thereby enhancing the film's wear resistance and hardness. However, when the addition exceeds a certain threshold, the surface rigidity of the film increases, resulting in reduced flexibility. Furthermore, the complete curing time is extended when the nano-CeO_2 content exceeds 2%. This occurs because increasing the nano-CeO_2 concentration raises the film's opacity, which slows the curing process.

Infrared Spectroscopy Analysis of Hybrid Coating

The Fourier transform infrared spectra of coatings containing different amounts of nano-CeO_2 (0%, 1%, 2%, 3%, and 4%) are shown in Figure 8. At 3400 cm^{-1}, an absorption peak corresponding to the vibration of amino groups is observed. As the nano-CeO_2 content increases, the intensity of the amino group stretching vibration peak also increases. At 2815 cm^{-1}, a characteristic stretching vibration absorption peak of methyl groups is present, and at 2720 cm^{-1}, a characteristic stretching vibration absorption peak of methylene groups is detected. The absorption peak at 1614 cm^{-1} is attributed to the characteristic stretching vibration of alkenes. A new absorption peak emerges at 617 cm^{-1}, corresponding to the characteristic absorption of the Ce–O bond, further confirming the successful preparation of the hybrid coating.

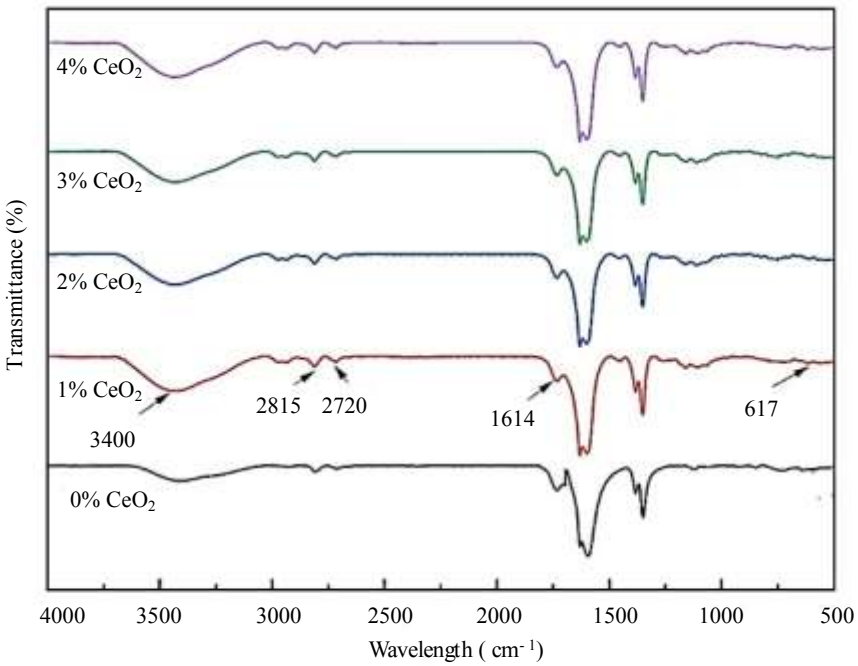

Figure 8. Effect of different HEA content on conversion rate of curing reaction.

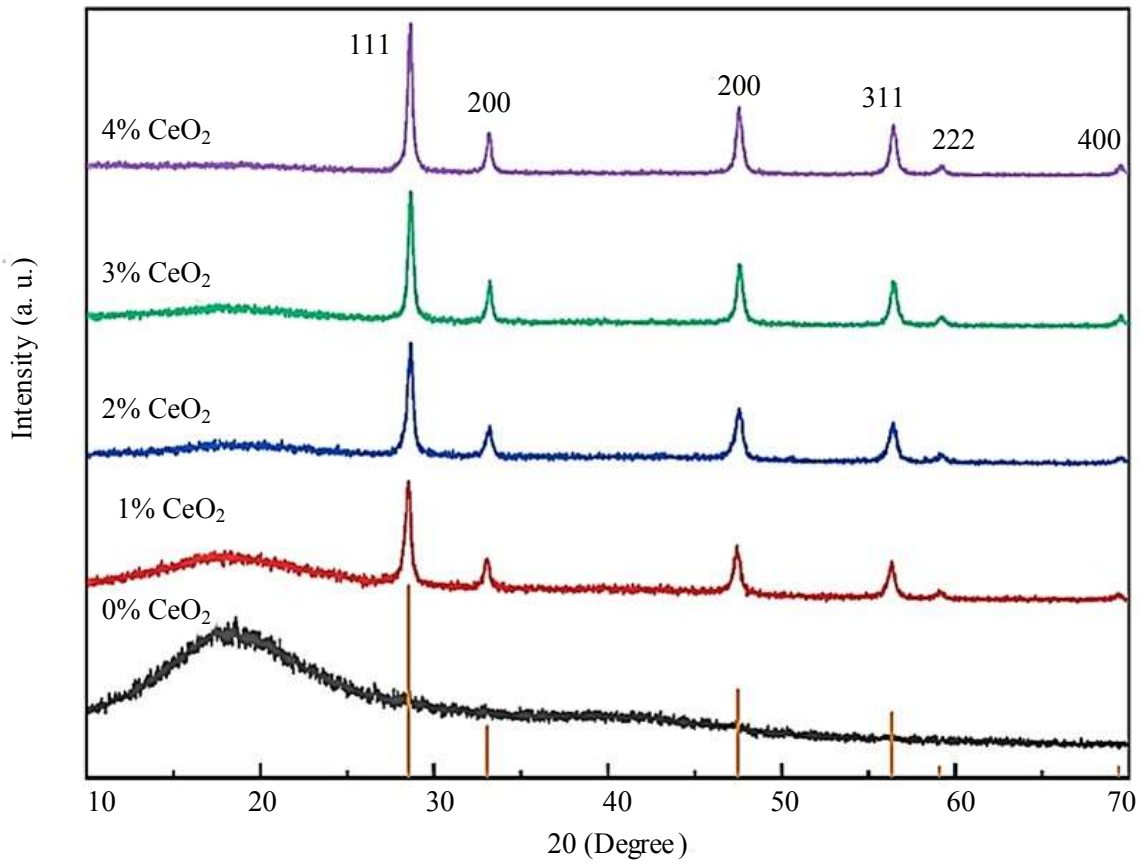

Figure 9. Infrared spectrum of the hybrid coating.

XRD Analysis of the Cured Coating

The XRD spectra of coatings containing different amounts of nano-CeO_2 (0%, 1%, 2%, 3%, and 4%) are shown in Figure 9. Diffraction peaks are observed at 2θ = 28.5°, 33.1°, 47.4°, 56.3°, 59.1°, and 69.4°, corresponding to the standard CeO_2 PDF card. As the nano-CeO_2 content increases, the peak intensity also increases. The diffraction peaks remain clear and sharp, with no impurity peaks, indicating that the modified CeO_2 retains good crystallinity within the hybrid coating.

Thermogravimetric Analysis of the Hybrid Coating

Figure 10 presents the thermogravimetric analysis of organic coatings containing different amounts of CeO_2. The thermal decomposition process of the hybrid coating from 0°C to 800°C can be divided into two stages. The first stage, occurring between 35°C and 350°C, involves weight loss primarily due to the evaporation of free and bound water molecules or residual organic solvents in the hybrid coating, with a weight loss rate of approximately 1.5%. The second stage, from 350°C to 500°C, is marked by significant weight loss resulting from the decomposition of the organic components in the hybrid coating. Furthermore, as the nano-CeO_2 content increases, the thermal stability of the hybrid coating improves. This enhancement is attributed to the formation of new chemical bonds between nano-CeO_2 and the organic components, which reinforces the stability of the coating.

SEM Analysis of the Hybrid Coating

Figure 11 presents the SEM images of coatings containing 4% commercially available nano-CeO_2 and 4% sol–gel-synthesized nano-CeO_2. The results show that although the sol–gel-synthesized nano-CeO_2 exhibits some agglomeration, it is less pronounced than that observed with commercially available nano-CeO_2. The improved stability of the sol–gel-synthesized nano-CeO_2 in the coating system can be attributed to its smaller particle size.

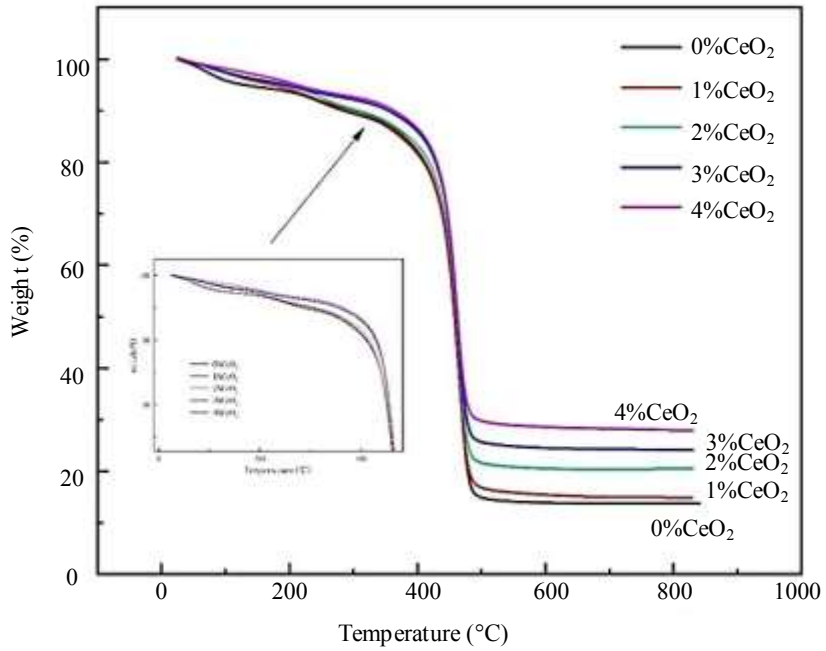

Figure 10. Infrared spectrum of the hybrid coating.

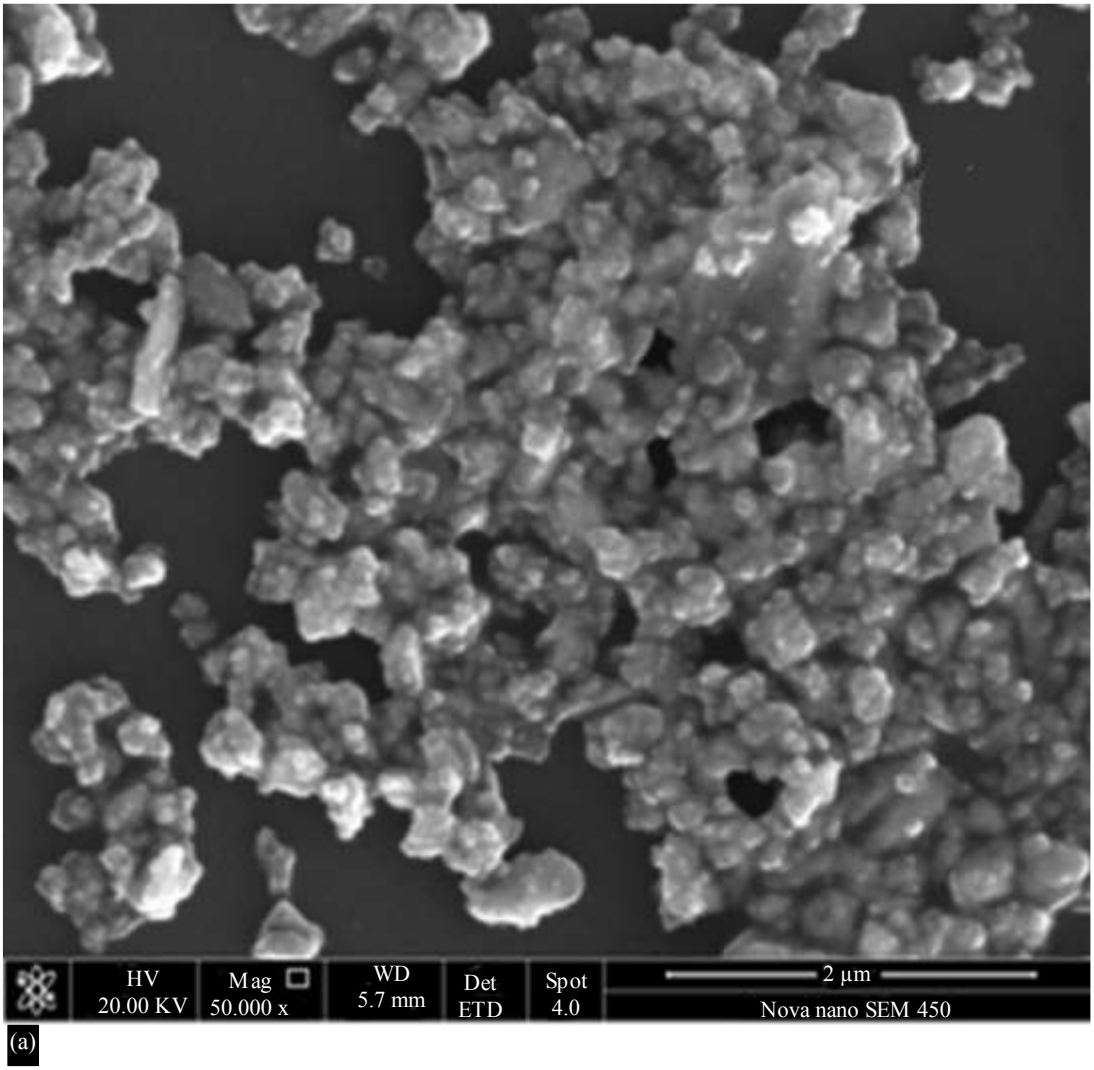

(a)

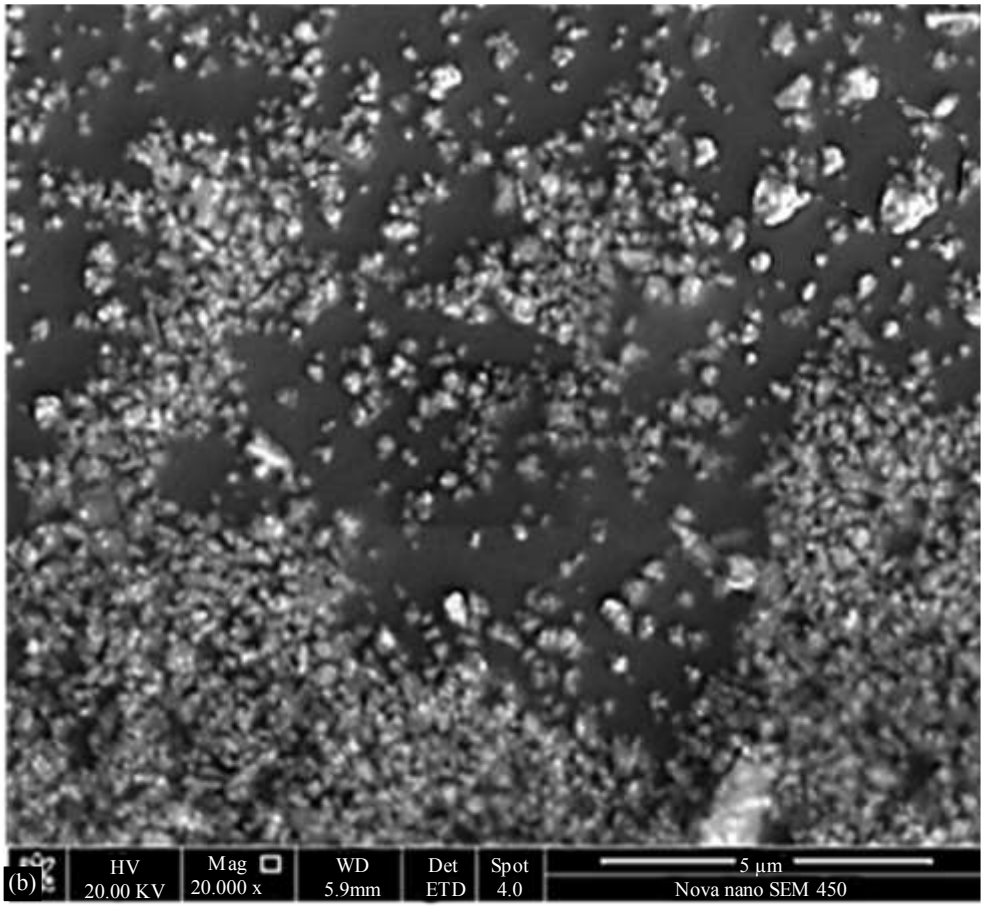

Figure 11. XRD analysis of the hybrid coating.

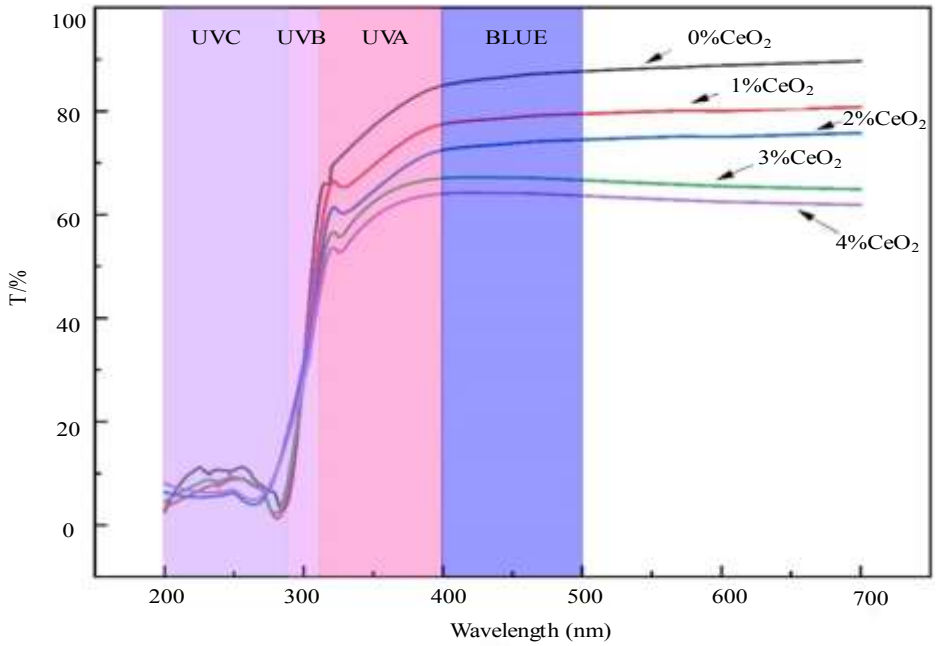

Figure 12. Optical performance study of the hybrid coating.

Optical Performance Analysis of the hybrid Coating

Figure 12 presents the optical performance analysis of organic/inorganic hybrid coatings containing 3% and 4% sol–gel-synthesized nano-CeO_2. The coating thickness was maintained at 3 µm, and the

light transmittance in the 200–700 nm wavelength range was measured using a UV–Vis spectrophotometer. As shown in Figure 10, when the nano-CeO_2 content is 3%, the coating's shielding rate for blue light (400–500 nm) is approximately 21%, for UVA (315–400 nm) it ranges from 23% to 40%, and for UVB (280–315 nm) it ranges from 40% to 89%. When the nano-CeO_2 content is increased to 4%, the shielding rate for blue light (400–500 nm) rises to about 34%, for UVA (315–400 nm) to 34–48%, and for UVB (280–315 nm) to 45–92%. This results attrbbute to the light absorption mechanism of Cerium Oxide. Cerium oxide is a wide bandgap semiconductor. The valence band (VB) is mainly composed of 2p orbitals of oxygen, while the conduction band (CB) is mainly composed of 4f and 5d orbitals of cerium. Band gap energy: The band gap width (Eg) of cerium oxide is approximately 3.0-3.4 eV (slightly different literature). Absorption process: When the energy of the incident photon (E=h ν) is greater than or equal to this bandgap energy, the photon will be absorbed and excite an electron in the valence band to the conduction band, forming an electron hole pair. This process is called intrinsic absorption or interband transition. According to the formula λ (nm)=1240/Eg (eV), the corresponding photon wavelength with a bandgap of 3.2 eV is approximately 388 nm, which is in the ultraviolet (UV) region. That's why cerium oxide nanoparticles are excellent UV absorbers. On the other hand, the most prominent feature of cerium oxide is its non-stoichiometry, which easily forms oxygen vacancies, which play a decisive role in its light absorption and reflection properties. There are two stable valence states for cerium ions in cerium oxide: Ce^{4+} and Ce^{3+}. Ce^{4+} can capture an electron and reduce it to Ce^{3+}. To maintain electrical neutrality, a positively charged oxygen vacancy ($Vo\cdot\cdot$) is generated in the crystal. $2\,Ce^{4+}+O^{2-} \rightarrow 2\,Ce^{3+}+Vo\cdot+189O_2\uparrow$. Introducing defect energy levels: These oxygen vacancies will introduce defect energy levels (or localized states) in the wide bandgap, which are located between the valence band top and the conduction band bottom. Electrons in the valence band can not only transition to the conduction band, but also to these defect energy levels; Similarly, electrons at defect energy levels can also transition to the conduction band. The energy required for these transitions is less than the bandgap energy. Due to the introduction of defect energy levels, the absorption edge of cerium oxide undergoes a red shift, allowing it to absorb not only ultraviolet light but also a portion of visible light (especially blue violet light).

CONCLUSIONS

When the amount of nano-CeO_2 added is 4%, the coating exhibits a shielding rate of approximately 34% for visible light (400–700 nm), 34–48% in the UVA (315–400 nm) region, and 45–92% in the UVB (280–315 nm) region. The coating demonstrates a hardness of 4H and an adhesion strength of 4B. The sol–gel method for modifying inorganic particles offers several advantages: it significantly reduces particle aggregation, enables uniform dispersion within the cured system, and allows processing at lower temperatures. Compared with other approaches, this method is both simple and efficient. The resulting product holds potential application value in eyewear, optical instruments, and optoelectronic devices.

Conflict of Interest

The authors declared that they have no conflicts of interest to this work.

REFERENCES

1. Bretterbauer, K.; Holzmann, C.; Rubatscher, E.; Schwarzinger, C.; Roessler, A.; Paulik, C., UV-curable coatings of highly crosslinked trimethylmelamine based acrylates and methacrylates. European Polymer Journal 2013, 49 (12), 4141-4148.
2. Liu, F.; Liu, A.; Tao, W.; Yang, Y., Preparation of UV curable organic/inorganic hybrid coatings-a review. Progress in Organic Coatings 2020, 145, 105685.
3. Yang, Z.; Wicks, D. A.; Hoyle, C. E.; Pu, H.; Yuan, J.; Wan, D.; Liu, Y., Newly UV-curable polyurethane coatings prepared by multifunctional thiol- and ene-terminated polyurethane aqueous dispersions mixtures: Preparation and characterization. Polymer 2009, 50 (7), 1717-1722.
4. Yang, Z.; Wicks, D. A.; Yuan, J.; Pu, H.; Liu, Y., Newly UV-curable polyurethane coatings prepared by multifunctional thiol- and ene-terminated polyurethane aqueous dispersions: Photopolymerization properties. Polymer 2010, 51 (7), 1572-1577.

5. Park, M.; Moon, H.; Jung, H. W.; Paik, H.-j.; Noh, S. M., Characteristics of Colorless Fluorinated Imide-Based Oligomers for UV-Curing Coatings. ACS Applied Polymer Materials 2024, 6 (17), 11039-11049.
6. Liu, F.; Wang, Y.; Xue, X.; Yang, H., UV curable EA-Si hybrid coatings prepared by combination of radical and cationic photopolymerization. Progress in Organic Coatings 2015, 85, 46-51.
7. Xu, T.; Zvonkina, I. J.; Soucek, M. D., UV-curable polyurethane inorganic–organic hybrid coatings. Journal of Coatings Technology and Research 2021, 18 (6), 1461-1479.
8. Xiao, T.; Geng, L.; Dai, Y.; Zhao, J.; Liu, C., UV-cured polymer aided phase change thermal energy storage: Preparation, mechanism and prospects. Journal of Energy Storage 2023, 64, 107066.
9. Akarsu, E.; Uslu, R., Light-activated hybrid organic/inorganic antimicrobial coatings. Journal of Sol-Gel Science and Technology 2018, 87 (1), 183-194.
10. Mano, I.; Taniguchi, J., Fabrication of an antireflection structure on an aspherical lens using a UV-curable inorganic–organic hybrid polymer. Japanese Journal of Applied Physics 2019, 58 (SD), SDDJ03.
11. Ma, Y.; Chen, L.; Ye, Y.; Wan, H.; Zhou, H.; Chen, J., Preparation and tribological behaviors of a novel organic-inorganic hybrid resin bonded solid lubricating coating cured by ultraviolet radiation. Progress in Organic Coatings 2019, 127, 348-358.
12. Manchanda, H.; Mannari, V., Super photo-base initiated organic-inorganic hybrid coatings by plural-cure mechanisms. Progress in Organic Coatings 2019, 127, 222-230.
13. Ma, H.; Zhou, L.; Han, C.; Zhang, C.; Zhang, L., The fabrication of novel optical diffusers based on UV-cured polymer dispersed liquid crystals. Liquid Crystals 2019, 46 (1), 138-144.
14. Quan, J.; Dong, T.; Shi, Z.; Xv, B.; Hu, H.; Hao, S.; Fan, H.; Huang, X.; Fan, M.; Cheng, Q.; Hang, Z., Development and characteristics of UV-photocurable anticorrosive MXene coatings. AIP Advances 2024, 14 (3) , 665.
15. Yamagishi, R.; Miura, S.; Yabu, K.; Ando, M.; Hachikubo, Y.; Yokoyama, Y.; Yasuda, K.; Takei, S., Fabrication Technology of Self-Dissolving Sodium Hyaluronate Gels Ultrafine Microneedles for Medical Applications with UV-Curing Gas-Permeable Mold. Gels 2024, 10 (1), 65.
16. Barman, B. K.; Sele Handegård, Ø.; Hashimoto, A.; Nagao, T., Carbon Dot/Cellulose-Based Transparent Films for Efficient UV and High-Energy Blue Light Screening. ACS Sustainable Chemistry & Engineering 2021, 9 (29), 9879-9890.
17. Li, Y.; Bian, X.; Wu, W.; Dong, H., Synthesis, characterization, and double shielding performance for ultraviolet and short-wave blue light of ceria-based materials. Ceramics International 2024, 50 (22, Part C), 48592-48599.
18. Hsu, C.-H.; Liu, T.-X.; Hsieh, I.-C.; Han, P.; Lien, S.-Y., Blue-light shielding, hard and hydrophobic inorganic and organic silicon stack-films prepared on flexible substrates. Thin Solid Films 2016, 618, 146-150.
19. Wittawat, R.; Rittipun, R.; Jarasfah, M.; Nattaporn, B., Synthesis of ZnO/TiO2 spherical particles for blue light screening by ultrasonic spray pyrolysis. Materials Today Communications 2020, 24, 101126.
20. Yang, Y.; Ju, Y.; Li, Y.; Yin, L.; Chen, L.; Gu, P.; Zhang, J., Transparent Nanostructured BiVO4 Double Films with Blue Light Shielding Capabilities to Prevent Damage to ARPE-19 Cells. ACS Applied Materials & Interfaces 2020, 12 (18), 20797-20805.
21. Su, K.; Tao, Y.; Zhang, J., Highly transparent plasticized PVC composite film with ideal ultraviolet/high-energy short-wavelength blue light shielding. Journal of Materials Science 2021, 56 (30), 17353-17367.
22. Liu, X.; Zhou, Q.; Lin, H.; Wu, J.; Wu, Z.; Qu, S.; Bi, Y., The Protective Effects of Blue Light-Blocking Films With Different Shielding Rates: A Rat Model Study. Translational Vision Science & Technology 2019, 8 (3), 19-19.
23. Han, C.; Wang, F.; Gao, C.; Liu, P.; Ding, Y.; Zhang, S.; Yang, M., Transparent epoxy–ZnO/CdS nanocomposites with tunable UV and blue light-shielding capabilities. Journal of Materials Chemistry C 2015, 3 (19), 5065-5072.
24. Li, H.; Wang, J.; Yang, J.; Zhang, J.; Ding, H., Large CeO2 nanoflakes modified by graphene as barriers in waterborne acrylic coatings and the improved anticorrosion performance. Progress in Organic Coatings 2020, 143, 105607.

25. Rajendran, P.; Muthuraj, A.; Rajagounder, N. E., Review on CeO2-Based Corrosion Coatings. Transactions of the Indian Ceramic Society 2022, 81 (4), 158-174.
26. Liu, K.-Q.; Kuang, C.-X.; Zhong, M.-Q.; Shi, Y.-Q.; Chen, F., Synthesis, characterization and UV-shielding property of polystyrene-embedded CeO2 nanoparticles. Optical Materials 2013, 35 (12), 2710-2715.
27. Zhao, Y.; Shi, L.; Tang, A.; Song, N.; Tang, S.; Ding, P., Enhanced blue light shielding property of light-diffusion polycarbonate composites by CeO2-coated silicate microspheres. Functional Materials Letters 2015, 08 (06), 1550074.
28. Paier, J.; Kropp, T.; Penschke, C.; Sauer, J., Stability and migration barriers of small vanadium oxide clusters on the CeO2(111) surface studied by density functional theory. Faraday Discussions 2013, 162 (0), 233-245.
29. Chang, S.; Bao, H.; Huang, W., Size-Dependent Redispersion or Agglomeration of Ag Clusters on CeO2. The Journal of Physical Chemistry C 2022, 126 (28), 11537-11543.
30. Kravtsov, A. A.; Chikulina, I. S.; Tarala, V. A.; Evtushenko, E. A.; Shama, M. S.; Tarala, L. V.; Malyavin, F. F.; Vakalov, D. S.; Lapin, V. A.; Kuleshov, D. S., Novel synthesis of low-agglomerated YAG:Yb ceramic nanopowders by two-stage precipitation with the use of hexamine. Ceramics International 2019, 45 (1), 1273-1282.
31. Waseem, S.; Zeeshan, T.; Tariq, H.; Majid, F.; Ali, M. D.; Kayani, Z. N.; Amami, M., The influence of transition metals (Fe, Co) on the structural, magnetic and optical properties of TiO2 nanoparticles synthesized by the hydrothermal method. Applied Physics A 2022, 128 (8), 690.
32. Predoana, L.; Stanciu, I.; Anastasescu, M.; Calderon-Moreno, J. M.; Stoica, M.; Preda, S.; Gartner, M.; Zaharescu, M., Structure and properties of the V-doped TiO2 thin films obtained by sol–gel and microwave-assisted sol–gel method. Journal of Sol-Gel Science and Technology 2016, 78 (3), 589-599.
33. Guha, A., Mathur, H., Malik, H., Enhancing grid resilience with hybrid STATCOM and optimal power flow control for renewable integration, Ain Shams Engineering Journal, 2024, 15(9): 102759. / doi.org/10.1016/j.asej.2024.102759.
34. Naveenkumar R., Shaik S., Suresh, S., Khan, M., Alruban, A., Otaibi, S., Performance enhancement of a solar still desalination system using activated carbon derived from sugarcane biomass, Ain Shams Engineering Journal, 2024, 15(8): 102759. / doi.org/10.1016/j.asej.2024.102759.
35. Lopes, Ana., Silva, J., Machado, J., Ramalho A., Soares, F., Mechanical and Microstructural Characterization of Carbon Fiber Reinforced Polymers Produced by Additive Manufacturing, Fibers 2022, 10 (4): 32. / doi.org/10.3390/fib10040032.
36. Li, Y., Wang, Y., Li, C., He, Y., Jiang, H., Zhang, Y., Song, Y., Zheng Q., A self-healing hydrogel based on polyacrylamide and sodium alginate with mechanical and swelling properties tuned via cross-linking density. Journal of Polymer Research, 2024, 71, doi.org/10.1007/s10965-024-03946-0.
37. Rahman, M., Khusairy M., Bakri, B., Hamdan, S., Rahman M., Mechanical and Dynamic Properties of Bamboo Fiber-Reinforced Polypropylene Composites, Journal of Composites Science 2023, 7(4): 136. /10.3390/jcs7040136
38. Shyu, J.-J.; Huang, Y.-H., Development of blue-light absorbing silicate glasses through codoping with TiO2, CeO2, Fe2O3, and Bi2O3. Optical Materials 2024, 155, 115899.
39. Wang, W.; Zhang, B.; Jiang, S.; Bai, H.; Zhang, S. Use of CeO2 Nanoparticles to Enhance UV-Shielding of Transparent Regenerated Cellulose Films Polymers, 2019, doi.org/10.3390/polym11030458.
40. Li, P.; Zou, G.; Chang, L.; Guo, W.; Tian, K.; Li, X.; Wang, H., UV-stimulated self-healing SiO2/CeO2 microcapsule with excellent UV-blocking capability in epoxy coating. Bulletin of Materials Science 2023, 46 (3), 159.
41. Rahman, M. M.; Suleiman, R.; Zahir, M. H.; Helal, A.; Kumar, A. M.; Haq, M. B. Multi Self-Healable UV Shielding Polyurethane/CeO2 Protective Coating: The Effect of Low-Molecular-Weight Polyols Polymers, 2020, doi.org/10.3390/polym12091947.

